Charge/mass dynamic structure factors of water and applications to dielectric friction and electroacoustic conversion

Felix Sedlmeier,[1] Shahriar Shadkhoo,[2] Robijn Bruinsma,[2] and Roland R. Netz[3]
[1]*Physik Department, Technische Universität München, 85748 Garching, Germany*
[2]*Department of Physics and Astronomy, University of California, Los Angeles, Los Angeles, California 90095, USA*
[3]*Fachbereich Physik, Freie Universität Berlin, 14195 Berlin, Germany*

(Received 18 November 2013; accepted 13 January 2014; published online 6 February 2014)

We determine time correlation functions and dynamic structure factors of the number and charge density of liquid water from molecular dynamics simulations. Using these correlation functions we consider dielectric friction and electro-acoustic coupling effects via linear response theory. From charge-charge correlations, the drag force on a moving point charge is derived and found to be maximal at a velocity of around 300 m/s. Strong deviations in the resulting friction coefficients from approximate theory employing a single Debye relaxation mode are found that are due to non-Debye-like resonances at high frequencies. From charge-mass cross-correlations the ultrasonic vibration potential is derived, which characterizes the conversion of acoustic waves into electric time-varying potentials. Along the dispersion relation for normal sound waves in water, the ultrasonic vibration potential is shown to strongly vary and to increase for larger wavelengths. © *2014 AIP Publishing LLC*. [http://dx.doi.org/10.1063/1.4863444]

I. INTRODUCTION

The dynamic structure factor $S(\vec{k}, \omega)$ contains ample information on the structure and dynamics of condensed-matter systems. For water, where each molecule consists of one oxygen and two hydrogen atoms, various structure factors can be defined. The oxygen-oxygen structure factor S_{OO} is the dominant quantity for X-ray scattering experiments: Since X-rays interact predominantly with the electrons, the electron density is the relevant density related to the scattering cross section. In liquid water, due to the high electronegativity of the oxygen atom, the electron density is mainly centered around the oxygen atom and therefore one can determine the scattering cross section to a good approximation from the oxygen-oxygen structure factor using an isotropically averaged form factor,[1,2] which can be conveniently obtained from quantum chemistry calculations.[3] The recent usage of high intensity third generation synchrotron sources for inelastic X-ray scattering makes it possible to measure $S(\vec{k}, \omega)$ for water over a wide range of wave vectors and frequencies[4] from which Green's functions and interfacial water dynamics have been reconstructed.[5] An interesting result of the inelastic scattering studies was that the excitation spectrum of water is richer than that of simple liquids, which is dominated by Rayleigh and Brillouin scattering. Water has two pronounced peaks in $S(k, \omega)$ with ω in the meV range and k in the inverse Angstrom range that are absent in simple liquids.

Neutrons on the other hand interact predominantly with the atomic nuclei, and have a high scattering cross section for hydrogen atoms. To model neutron scattering experiments one therefore has to take into account additionally the oxygen-hydrogen and hydrogen-hydrogen structure factors S_{OH} and S_{HH}.[2] For the case of acoustic perturbations, which are associated with mass displacements, the center of mass density structure factor $S_{\rho\rho}$ is relevant,[6] while electrostatic fluctuations and correlations are embodied in the charge density structure factor S_{qq}, which determines also the solvation and dynamics of charged particles in water, like ions and electrons. In classical simulations, the structure factors $S_{\rho\rho}$ and S_{qq} can be constructed to a good approximation from the three site-site structure factors S_{OO}, S_{OH}, and S_{HH}, which therefore contain the complete structural and dynamical knowledge on the pair-correlation level. The importance of structure factors is due to a large extent to the fact that they are related to the linear response functions via the fluctuation dissipation theorem.[7] If, for example, one knows the charge density structure factor S_{qq} then one can directly obtain the imaginary part of the dielectric response function. This provides us with the polarization response of the medium to an external charge or potential distribution. To give an explicit application, the Bethe formula relates the stopping power of water for an electron to the dielectric response function of water.[8]

A less familiar quantity is the cross-correlation structure factor $S_{\rho q}$, which, for example, describes the coupling between electrostatic and acoustic effects. Such a coupling was first studied by Debye[9] who predicted that in electrolyte solutions an ultrasonic wave induces an alternating electrostatic potential, the so-called ultrasonic vibration potential (UVP) ϕ_{UVP}. The first experimental proof of this phenomenon was provided by Yeager *et al.*[10] and it has been used since as a versatile method to determine ionic partial molar volumes (see, e.g., Ref. 11 and references therein). Based on the observation that the UVP signal increases with decreasing salt concentrations, it was suggested by Hunter *et al.*[12,13] that also pure water might generate an UVP. A phenomenological theory for the UVP of polar liquids has been subsequently developed

by Weinman.[14,15] Although Zana and Yeager[11] argued that the observed increase in UVP with decreasing salt concentration can be explained by piezoelectric effects associated with the electrodes used to measure the UVP, the question whether neat polar liquids like water can generate a UVP is still unsettled. The reverse effect, that is the generation of an acoustic wave by the application of a time-varying electric field, quantified by the electrokinetic sonic amplitude (ESA), also exists and has been first measured by Oja *et al.*[16]

In this work we determine the auto and cross-correlation functions and associated dynamic structure factors of the oxygen and hydrogen sites in liquid water over a wide range of wave vectors and frequencies. From those functions we derive diagonal and off-diagonal structure factors involving mass and charge densities. Based on these general results we focus on two different phenomena:

(i) From the charge-charge dynamic structure factor we derive the dielectric friction force on a moving point charge via linear response theory. As a function of the point charge velocity, the drag force exhibits a pronounced maximum around a velocity of the order of 300 m/s. When compared with the standard theory for the friction of an electron in liquid water that employs a single Debye relaxation mode approximation,[17,18] we find friction forces that are considerably larger. This deviation is due to non-Debye-like resonances at high frequencies in the simulated water susceptibility. The good agreement between single-Debye mode theory and experimental data for the electron mobility in water is nevertheless retained since the high-frequency domain is effectively preempted by a high-momentum cutoff that in a crude manner accounts for dielectric saturation effects. However, these non-Debye effects might be relevant for the kinetics and motion of partial molecular charges.

(ii) We investigate electro-acoustic coupling effects using the charge-mass dynamic structure factor and derive explicit values for the conversion coefficient in liquid water. When we calculate the ultrasonic vibration potential along the dispersion relation for normal sound waves in water, we find a strong dependence on the wavelength, which is experimentally relevant.

In Sec. II we describe in detail the molecular dynamics (MD) methodology used in this work. We discuss the definitions and results for the various dynamic correlation functions and structure factors in Sec. III. In Sec. IV we use linear response theory to determine the velocity-dependent drag force on a charged particle and in Sec. V we determine the electro-acoustic conversion coefficient.

II. MOLECULAR DYNAMICS SIMULATIONS

Molecular dynamics simulations are performed using the Gromacs simulation package.[19,20] Throughout this study, the SPC/E[21] water model is used, which consists of three point charges arranged in a fixed geometry with partial charges $z_H = +0.4238$ on the hydrogen atoms and $z_O = -0.8476$ on the oxygen atom. Dispersion interactions between the water molecules are modeled by a Lennard-Jones interaction centered on the oxygen atom.

We consider systems of two different sizes: The smaller system consists of 895 water molecules in a cubic box with periodic boundary conditions. At $T = 300$ K this corresponds to a box size of roughly $3.0 \times 3.0 \times 3.0\,\mathrm{nm}^3$. We perform simulations at a temperature of $T = 300$ K and at a pressure of $p = 1$ bar. The system is equilibrated first in a NVT ensemble (constant particle number, volume, and temperature) for $t = 50$ ps and then in a NPT ensemble (constant particle number, pressure, and temperature) for $t = 10$ ns, in order to determine the box size corresponding to the pressure of $p = 1$ bar. The box size is then set to the average obtained in the NPT simulation and after an additional equilibration of $t = 50$ ps production runs are performed in the NVT ensemble for $t = 0.4$ ns. Configurations are saved with the full time resolution of $\delta t = 0.002$ ps. Additionally, longer simulations are run for $t = 2.0$ ns and configurations are saved with a time resolution of $\delta t = 0.01$ ps. To determine the heat capacities at constant volume c_v and constant pressure c_p, which we need to derive the sound velocity in a consistent manner, additional simulations at temperatures of $T = 280$ K and 320 K are performed in the NVT and NPT ensembles for $t = 10$ ns, respectively.

To reach lower wave vectors and to obtain a better resolution of the low-wave vector region of the dynamic structure factor, we also simulate a larger system containing ≈33 000 water molecules, which corresponds to a box size of $10 \times 10 \times 10\,\mathrm{nm}^3$, in the NVT ensemble for $t = 2.0$ ns, where configurations are saved each $\delta t = 0.01$ ps, after equilibration in the NPT ensemble for $t = 2.0$ ns.

A Berendsen weak coupling thermostat and barostat[22] with a relaxation time of $\tau = 1.0$ ps is used for temperature and pressure control. All non-bonded interactions are cutoff at a radius of $r_c = 0.9$ nm. Long-range electrostatic interactions are treated by the particle mesh Ewald method[23,24] with tinfoil boundary conditions. For the Lennard-Jones interaction an analytic long-range correction is applied to energy and pressure.[25] The bonds and angles in the water molecules are kept fixed using the analytic SETTLE algorithm,[26] and a timestep of 2 fs is used for the integration of the equations of motion.

III. DYNAMIC STRUCTURE FACTORS

We define the auto- and cross-correlation functions of the particle number and charge densities in reciprocal space as

$$F_{\alpha\beta}(\vec{k}, t) = \frac{1}{N}\langle \alpha(\vec{k}, t)\beta^*(\vec{k}, 0)\rangle, \tag{1}$$

where $\alpha, \beta = \mathrm{O}, \mathrm{H}, \rho, q$. For $\alpha = \mathrm{O}, \mathrm{H}, \rho$

$$\alpha(\vec{k}, t) = \sum_{i=1}^{N} e^{-i\vec{k}\cdot\vec{r}_i^{\alpha}(t)}, \tag{2}$$

denotes the Fourier transform of the oxygen, hydrogen, and molecule number density, while

$$q(\vec{k}, t) = e\sum_{i=1}^{N}\sum_{\alpha=O,H,H} z_\alpha e^{-i\vec{k}\cdot\vec{r}_i^{\alpha}(t)} \tag{3}$$

is the Fourier transform of the charge density. Here, z_α and $\vec{r}_i^{\,\alpha}(t)$ are the partial charge and the position of the atomic site $\alpha = \mathrm{O}, \mathrm{H}$ while $\vec{r}_i^{\,\rho}(t)$ is the position of the center of mass of the ith water molecule. The total number of water molecules is N, X^* denotes the complex conjugate of X and e is the elementary charge. The density-density autocorrelation function $F_{\rho\rho}(\vec{k}, t)$ is also called the intermediate scattering function. The static structure factor is the $t \to 0$ limit of the correlation function, i.e., $S_{\alpha\beta}(\vec{k}) = F_{\alpha\beta}(\vec{k}, 0)$ for $\alpha, \beta = \mathrm{O}, \mathrm{H}, \rho, q$. The dynamic structure factor $S_{\alpha\beta}(\vec{k}, \omega)$ is the Fourier transform of the correlation function,

$$S_{\alpha\beta}(\vec{k}, \omega) = \frac{1}{2\pi} \int_{-\infty}^{\infty} F_{\alpha\beta}(\vec{k}, t) e^{i\omega t} dt. \tag{4}$$

The structure factor $S_{\alpha\beta}(\vec{k}, \omega)$ can be calculated from a simulation trajectory either by Eq. (4) or from the alternative expression,

$$S_{\alpha\beta}(\vec{k}, \omega) = \frac{1}{2\pi} \langle \alpha_{\Delta t}(\vec{k}, \omega) \beta^*_{\Delta t}(\vec{k}, \omega) \rangle / (N \Delta t), \tag{5}$$

where the Fourier transform of the densities for the observation interval Δt is defined by

$$\alpha_{\Delta t}(\vec{k}, \omega) = \int_0^{\Delta t} \alpha(\vec{k}, t) e^{i\omega t} dt. \tag{6}$$

The charge density correlation functions can be expressed in terms of the site-site correlation functions as follows:

$$F_{qq} = e^2 z_{\mathrm{H}}^2 (4F_{\mathrm{OO}} - 4F_{\mathrm{OH}} + F_{\mathrm{HH}}), \tag{7}$$

$$F_{\mathrm{O}q} = e z_{\mathrm{H}} (-2F_{\mathrm{OO}} + F_{\mathrm{OH}}). \tag{8}$$

The static structure factors $S_{\rho\rho}(k)$, $S_{qq}(k)$, $S_{\mathrm{O}q}(k)$, and $S_{\rho q}(k)$ and the static site-site structure factors $S_{\mathrm{OO}}(k)$, $S_{\mathrm{OH}}(k)$, and $S_{\mathrm{HH}}(k)$ are shown in Fig. 1. It is seen that $S_{\rho\rho}(k)$ (filled black circles) and $S_{\mathrm{OO}}(k)$ (open black circles) on the one hand and $S_{\rho q}$ (filled blue triangles) and $S_{\mathrm{O}q}(k)$ (open blue triangles) on the other hand almost perfectly overlap with each other. This reflects the fact that due to the small mass of H there is practically no difference between the oxygen and the center of mass positions in a water molecule. In the dynamic case there are distinct differences, as will be discussed below. The static site-site correlation functions $S_{\mathrm{OO}}(k)$, $S_{\mathrm{OH}}(k)$, and $S_{\mathrm{HH}}(k)$ are shown in Fig. 1(b) normalized by their respective site multiplicities. With this normalization they converge towards the same value in the long wavelength (small k) limit, since in this limit the small differences in the atomic positions are negligible with respect to the molecular position.

Figure 2 shows the autocorrelation functions $F_{\rho\rho}(k, t)$, $F_{\mathrm{OO}}(k, t)$, and $F_{qq}(k, t)$ and the corresponding dynamic structure factors $S_{\mathrm{OO}}(k, \omega)$, $S_{\rho\rho}(k, \omega)$, and $S_{qq}(k, \omega)$, while Fig. 3 shows the cross-correlation functions $F_{\mathrm{O}q}(k, t)$ and $F_{\rho q}(k, t)$ and the corresponding dynamic structure factors $S_{\mathrm{O}q}(k, \omega)$ and $S_{\rho q}(k, \omega)$ for several values of $k = 3.5$, 10.5, 20.5, 28.5, and 37.5 nm^{-1}. Our results for the charge-charge correlation function compare well with the calculations of Ladany and Perng,[27] who also used the SPC/E water model. Similar results for $F_{qq}(k, t)$ and $S_{qq}(k, \omega)$ have also been obtained for the TIP4P[28] and the BJH[29] water models.

If one compares $F_{\mathrm{O}q}(k, t)$ with $F_{\rho q}(k, t)$ in Fig. 3 for $k = 3.5$ nm^{-1}, it is evident that the high frequency oscillations present in $F_{\mathrm{O}q}(k, t)$ at short times $t < 0.3$ ps are absent in $F_{\rho q}(k, t)$. Correspondingly, the peaks in $S_{\mathrm{OO}}(k, \omega)$ and $S_{\mathrm{O}q}(k, \omega)$ in Figs. 2 and 3 around $\omega \approx 175$ ps^{-1} are absent for $S_{\rho\rho}(k, \omega)$ or much weaker for $S_{\rho q}(k, \omega)$. These differences can be explained by *librational modes* of the water molecules. These are small rotations around an axis through the center of mass of the molecules, which are manifest in the motion of the oxygen atom but not in the center of mass motion. Note that the libration frequency obtained from an analysis of single-molecule orientational autocorrelation functions for SPC/E water is significantly smaller,[30] whether this difference is due to collective water effects remains to be clarified.

Site-site correlation functions $F_{\mathrm{OH}}(k, t)$ and $F_{\mathrm{HH}}(k, t)$ and the corresponding structure factors $S_{\mathrm{OH}}(k, \omega)$ and $S_{\mathrm{HH}}(k, \omega)$ are plotted in Fig. 4. Since $S_{\mathrm{OH}}(k, \omega)$ exhibits zero-crossings for several values of k we plot the absolute value.

Figures 5–8 show 2D contour plots of the logarithm of the dynamic structure factors $S_{\mathrm{OO}}(k, \omega)$, $S_{\rho\rho}(k, \omega)$, $S_{qq}(k, \omega)$, $|S_{\mathrm{O}q}(k, \omega)|$, and $|S_{\rho q}(k, \omega)|$ in the k-ω-plane. An enlarged view of the low-k and ω region for $S_{\mathrm{OO}}(k, \omega)$, obtained from simulations of a system containing ≈33 000 water molecules and a box size of $10 \times 10 \times 10$ nm^3, is shown in Fig. 6. Also indicated in Fig. 6 are the dispersion relations, $\omega(k) = c_s k$, of propagating sound waves for the hydrodynamic

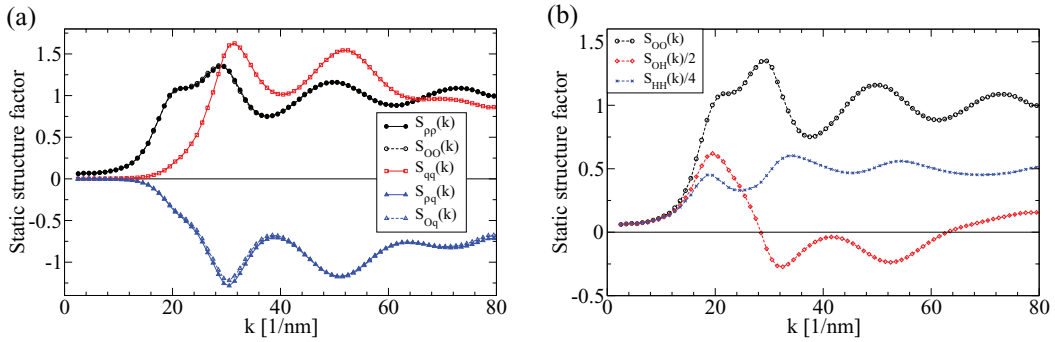

FIG. 1. (a) Static structure factors $S_{\rho\rho}(k)$ (filled black circles), $S_{\mathrm{OO}}(k)$ (open black circles), $S_{qq}(k)$ (red squares), $S_{\rho q}(k)$ (filled blue triangles), and $S_{\mathrm{O}q}(k)$ (open blue triangles). Note that $S_{\rho q}(k)$ and $S_{\mathrm{O}q}(k)$ are very similar, while $S_{\mathrm{OO}}(k)$ and $S_{\rho\rho}(k)$ are virtually indistinguishable. (b) Static site-site structure factors $S_{\mathrm{OO}}(k)$ (open black circles), $S_{\mathrm{OH}}(k)$ (red diamonds), and $S_{\mathrm{HH}}(k)$ (blue crosses), normalized by their respective site multiplicities. All data are obtained by MD simulations of SPC/E water at $T = 300$ K and $p = 1$ bar.

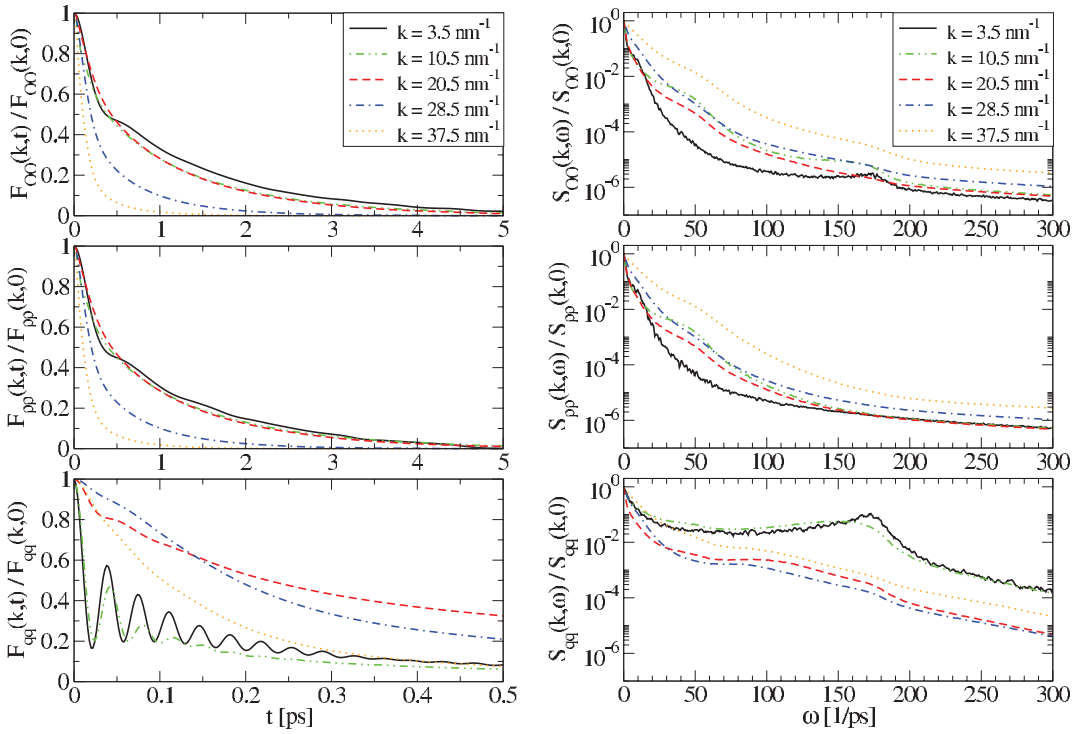

FIG. 2. *Left panels:* Normalized autocorrelation functions $F_{OO}(k, t)$, $F_{\rho\rho}(k, t)$, and $F_{qq}(k, t)$ for several values of the wave vector k. *Right panels:* Dynamic structure factors $S_{OO}(k, \omega)$, $S_{\rho\rho}(k, \omega)$, and $S_{qq}(k, \omega)$ normalized by the $\omega = 0$ value for several different wave vectors k. All data are obtained by MD simulations of SPC/E water at $T = 300$ K and $p = 1$ bar.

(dashed black line) and the hypothesized fast sound (dashed red line) modes.[31] The hydrodynamic (adiabatic) sound velocity is given by

$$c_s = \sqrt{\frac{\gamma}{\kappa_T \rho_m}}, \tag{9}$$

where $\gamma = c_p/c_v$ is the adiabatic index, κ_T is the isothermal compressibility, ρ_m is the mass density, and c_p and c_v are the isobaric and isothermal heat capacities of water. For the SPC/E water model at $T = 300$ K we obtain $c_p = 86.7$ J/(mol K) and $c_v = 83.7$ J/(mol K) from linearly fitting the temperature dependence of the enthalpy and energy, respectively, yielding $\gamma = 1.037$. With $\kappa_T = 45.5 \times 10^{-11}$ Pa^{-1} and $\rho_m = 0.999$ kg/l[32] we obtain $c_s = 1510$ m/s, which compares well with the experimental value of $c_s = 1484$ m/s.

The literature discussion on the fast sound mode has a long and lively history: From the analysis of the dynamic structure factor $S_{\rho\rho}(k, \omega)$ obtained by MD simulations of the ST2[33] water model Rahman and Stillinger[34] found two excitations, which they attributed to propagating modes

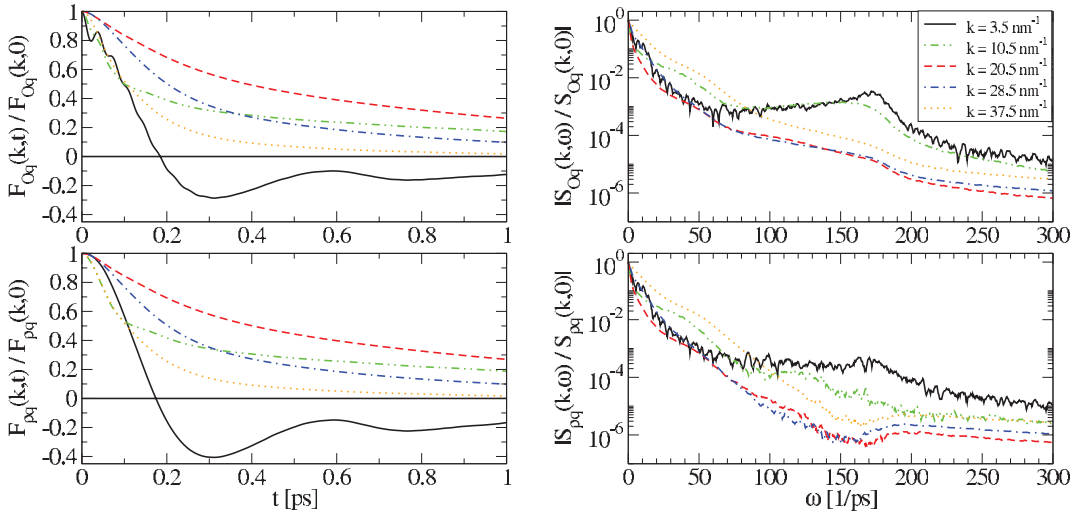

FIG. 3. *Left panels:* Normalized cross-correlation functions $F_{Oq}(k, t)$ and $F_{\rho q}(k, t)$ for several values of the wave vector k. *Right panels:* Dynamic structure factors $S_{Oq}(k, \omega)$ and $S_{\rho q}(k, \omega)$ normalized by the $\omega = 0$ value for several different wave vectors k. All data are obtained by MD simulations of SPC/E water at $T = 300$ K and $p = 1$ bar.

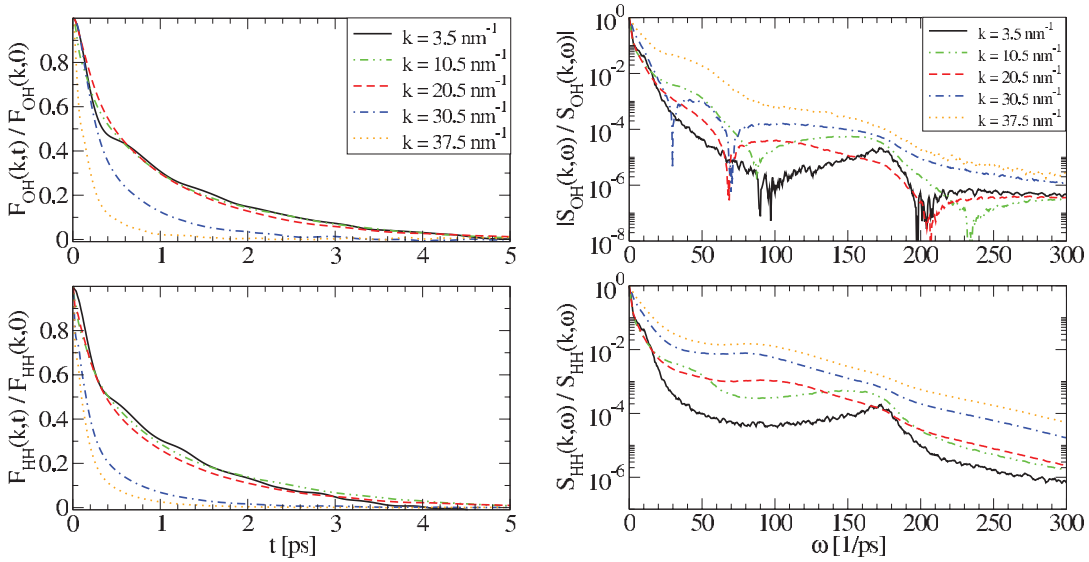

FIG. 4. *Left panels*: Normalized site-site time correlation functions for several values of the wave vector k. *Right panels:* Corresponding dynamic structure factors normalized by the $\omega = 0$ value for several values of the wave vector k. All data are obtained by MD simulations of SPC/E water at $T = 300$ K and $p = 1$ bar.

with sound velocities of ≈1500 m/s and ≈3000 m/s. Many experimental[35–38] and simulation[39–41] studies have been performed since then and the current opinion is that rather than having two coexisting excitation modes, the ordinary sound branch with a sound velocity of $c_s \approx 1500$ m/s exhibits a gradual transition to the fast sound dispersion with a sound velocity of $c_s' \approx 3500$ m/s[31] at higher wave vectors. In the k-range studied in this work, the Brillouin peak corresponding to the propagating sound wave is quite broad and overlaps with the central Rayleigh peak, which is due to diffusion of the water molecules. Consequently, it is only discernable as a slight shoulder and not as a pronounced maximum in $S_{OO}(k, \omega)$ and $S_{\rho\rho}(k, \omega)$ in Figure 2. The Rayleigh peak is reflected in Fig. 6(a) by the slight bulge in the contour lines in between the two dashed lines. As indicated in Fig. 6(b), with increasing wave vector k the position of the shoulder moves

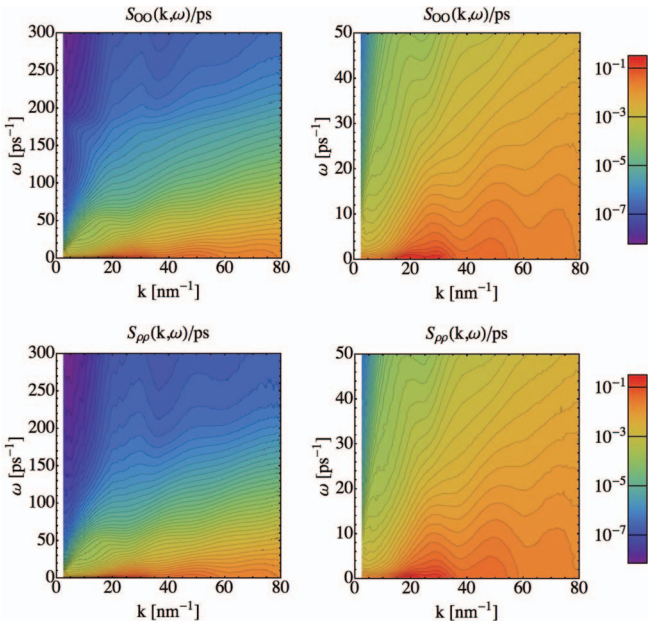

FIG. 5. *Left panels:* Dynamic structure factors $S_{OO}(k, \omega)$ (top row) and $S_{\rho\rho}(k, \omega)$ (bottom row) of SPC/E water at $T = 300$ K and $p = 1$ bar. *Right panels:* Close-up view of the low ω region.

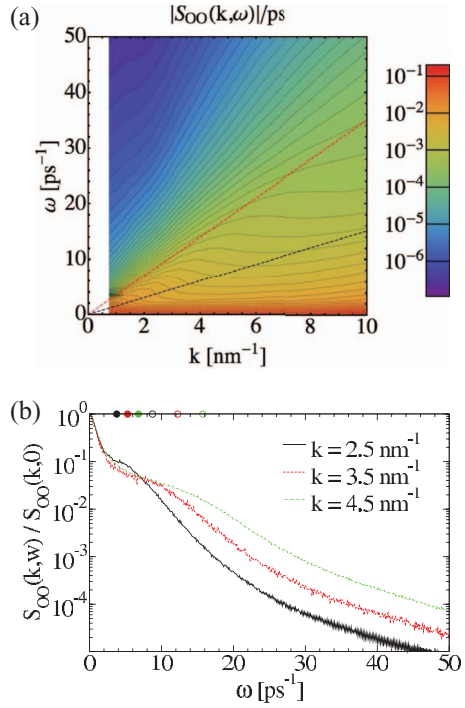

FIG. 6. (a) Low k and ω region of the dynamic structure factor $S_{OO}(k, \omega)$ of SPC/E water at $T = 300$ K and $p = 1$ bar, obtained from simulations of a system containing ≈33 000 water molecules with a box size of ≈10 × 10 × 10 nm^3. The black and red dashed lines indicate the dispersion relations of hydrodynamic and the hypothesized fast sound modes with sound velocities of $c_s = 1510$ m/s and $c_s = 3500$ m/s. (b) Normalized slices of $S_{OO}(k, \omega)$ at fixed $k = 2.5$, 3.5, and 4.5 nm^{-1}. Filled and open circles at the top boundary show the positions of the expected Brillouin peaks for the normal and fast sound velocities, respectively.

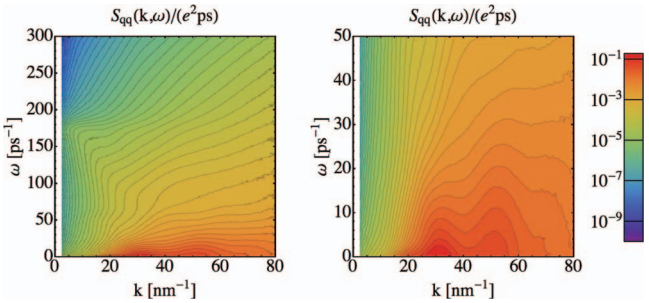

FIG. 7. *Left panel:* Dynamic charge-charge structure factor $S_{qq}(k, \omega)$ of SPC/E water at $T = 300$ K and $p = 1$ bar. *Right panel:* Close-up view of the low ω region.

from the position predicted by the dispersion relation of the normal sound c_s (filled spheres) towards the prediction of the dispersion relation for the fast sound c_s' (open spheres).

IV. ELECTRODYNAMIC EFFECTS

A. Linear response formalism

We briefly review here the basic definitions of electrodynamic linear response theory which we will need in the following (see, e.g., Refs. 29). The dielectric response tensor $\chi_{\alpha\beta}$ is defined by the non-local relation between the polarization density $\vec{P}$ at position $\vec{r}$ and time t and the dielectric displacement $\vec{D}$ at position $\vec{r}'$ and time t',

$$P_\alpha(\vec{r}, t) = \int_V d^3r' \int_{-\infty}^{t} dt' \chi_{\alpha\beta}(\vec{r} - \vec{r}', t - t') D_\beta(\vec{r}', t'). \tag{10}$$

For a homogeneous medium the corresponding expression in Fourier space is

$$P_\alpha(\vec{k}, \omega) = \chi_{\alpha\beta}(\vec{k}, \omega) D_\beta(\vec{k}, \omega). \tag{11}$$

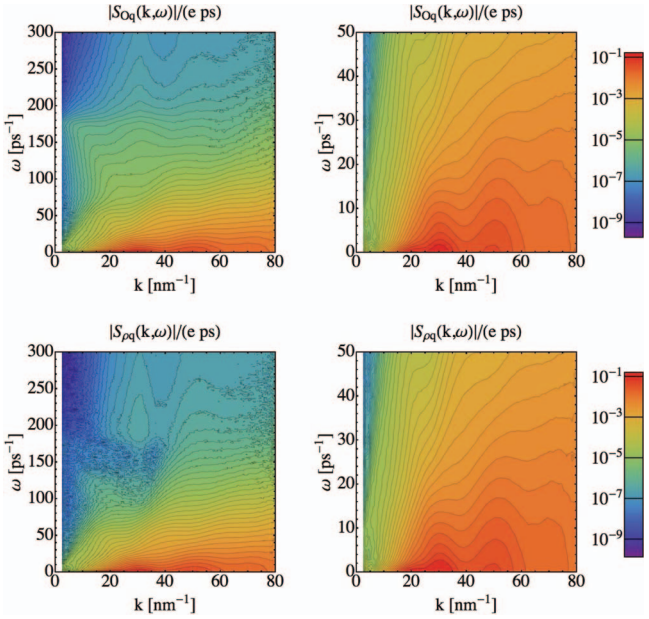

FIG. 8. *Left panels:* Dynamic structure factors $S_{Oq}(k, \omega)$ (top row) and $S_{\rho q}(k, \omega)$ (bottom row) of SPC/E water at $T = 300$ K and $p = 1$ bar. *Right panels:* Close-up view of the low ω region.

In an isotropic medium the response tensor can be decomposed into longitudinal and transversal parts,

$$\chi_{\alpha\beta}(\vec{k}, \omega) = \frac{k_\alpha k_\beta}{k^2} \chi_{||}(k, \omega) + \left(\delta_{\alpha\beta} - \frac{k_\alpha k_\beta}{k^2}\right) \chi_\perp(k, \omega), \tag{12}$$

with

$$\chi_{||}(k, \omega) = \frac{k_\alpha k_\beta}{k^2} \chi_{\alpha\beta}(\vec{k}, \omega), \tag{13}$$

$$\chi_\perp(k, \omega) = \left(\delta_{\alpha\beta} - \frac{k_\alpha k_\beta}{k^2}\right) \chi_{\alpha\beta}(\vec{k}, \omega). \tag{14}$$

The longitudinal response function is related to the charge density structure factor by the fluctuation dissipation theorem,[7]

$$\mathrm{Im}[\chi_{||}(k, \omega)] = \frac{\pi}{k^2} \frac{\rho}{\varepsilon_0 k_B T} \omega S_{qq}(k, \omega). \tag{15}$$

We further have

$$q_{\mathrm{ind}}(\vec{k}, \omega) = -\chi_{||}(k, \omega) q_{\mathrm{ext}}(\vec{k}, \omega), \tag{16}$$

where $q_{\mathrm{ext}}(\vec{k}, \omega)$ and $q_{\mathrm{ind}}(\vec{k}, \omega)$ are the Fourier transforms of an external and the induced charge density. In non-magnetic media and at low frequencies (which amounts to a quasistatic approximation), the transverse response function $\chi_\perp(k, \omega)$, does not enter the equations for the electrostatic potential, and will not be studied further in this work. It can be obtained directly from the polarization density correlation function.[29]

B. Dielectric friction and drag force on a point charge

Next, we derive an expression for the drag force on a charged point particle moving through a medium with velocity $\vec{v}$, using the linear response formalism. The external charge density arising from the moving point charge is $q_{\mathrm{ext}}(\vec{r}, t) = q_0 \delta(\vec{r} - \vec{v}t)$, where q_0 is the charge of the particle and $\delta(\vec{r})$ is the Dirac delta function. Accordingly, the external charge density in Fourier space is $q_{\mathrm{ext}}(\vec{k}, \omega) = 2\pi q_0 \delta(\vec{k} \cdot \vec{v} - \omega)$. The induced charge density follows from Eq. (16) as

$$q_{\mathrm{ind}}(\vec{k}, \omega) = -2\pi q_0 \chi_{||}(k, \omega) \delta(\vec{k} \cdot \vec{v} - \omega). \tag{17}$$

In the quasi-static approximation, the electric potential produced by the induced charge density is given by

$$\phi_{\mathrm{ind}}(\vec{k}, \omega) = \frac{1}{k^2} \frac{q_{\mathrm{ind}}(\vec{k}, \omega)}{\varepsilon_0} \tag{18}$$

$$= -\frac{1}{k^2} \frac{2\pi q_0}{\varepsilon_0} \chi_{||}(k, \omega) \delta(\vec{k} \cdot \vec{v} - \omega). \tag{19}$$

Applying the inverse Fourier transform, we obtain

$$\phi_{\mathrm{ind}}(\vec{r}, t) = -\int \frac{d\omega}{2\pi} \int \frac{d^3k}{(2\pi)^3} \phi_{\mathrm{ind}}(\vec{k}, \omega) e^{i(\vec{k}\cdot\vec{r} - \omega t)} \tag{20}$$

$$= -\int \frac{d^3k}{(2\pi)^3} \frac{q_0}{\varepsilon_0 k^2} \chi_{||}(k, \vec{k} \cdot \vec{v}) e^{i(\vec{k}\cdot\vec{r} - \vec{k}\cdot\vec{v}t)}. \tag{21}$$

The force on the moving particle due to the induced charge density then is $\vec{F} = -q_0 \nabla \phi_{\mathrm{ind}}(\vec{r}, t)|_{\vec{r}=\vec{v}t}$, which yields

$$\vec{F} = i \frac{q_0^2}{(2\pi)^3 \varepsilon_0} \int d^3k \frac{\vec{k}}{k^2} \chi_{||}(k, \vec{k} \cdot \vec{v}). \tag{22}$$

Without loss of generality we can assume $\vec{v} = v\vec{e}_z$ and write the integral in spherical coordinates,

$$\vec{F} = i\frac{q_0^2}{(2\pi)^3\varepsilon_0}\int_0^{2\pi} d\varphi \int_{-1}^{1} ds \int_0^{k_{\max}} dk\vec{k}\chi_{||}(k, kvs), \quad (23)$$

where $s = \cos\theta$ and we have introduced an upper wave vector cutoff $k_{\max}$ that will be discussed in detail later on.

It is easily seen, that the x and y components of $\vec{F}$ vanish and with $\vec{F} = F\vec{e}_z$ we obtain

$$F = i\frac{q_0^2}{(2\pi)^2\varepsilon_0}\int_{-1}^{1} ds \int_0^{k_{\max}} dkks\chi_{||}(k, kvs). \quad (24)$$

Splitting the response function into its real and imaginary parts as $\chi = \chi' + i\chi''$, one finds

$$\chi'(k, \omega) = \chi'(k, -\omega), \quad (25)$$

$$\chi''(k, \omega) = -\chi''(k, -\omega), \quad (26)$$

and therefore we obtain

$$F = -\frac{q_0^2}{(2\pi)^2\varepsilon_0}\int_{-1}^{1} ds \int_0^{k_{\max}} dkks\chi_{||}''(k, kvs). \quad (27)$$

The minus sign indicates here that the friction force F acts in a direction opposite to that of the velocity. As expected, only the imaginary part of the susceptibility contributes to the friction. Using Eq. (15) we can express the friction force in terms of the charge density structure factor alternatively as

$$F = -\frac{q_0^2\rho v}{4\pi\varepsilon_0^2 k_B T}\int_{-1}^{1} ds \int_0^{k_{\max}} dks^2 S_{qq}(k, kvs). \quad (28)$$

The same result appears as an intermediate step in the derivation of the Bethe stopping power.[42] Figure 9(a) shows the drag force F as a function of the point charge velocity v obtained by numerically integrating Eq. (28) using the dynamic charge-charge structure factor of SPC/E water at $T = 300$ K and $p = 1$ bar as shown in Fig. 7. Different curves show results for different values of the upper wave vector cutoff $k_{\max}$. We find a pronounced dependence on $k_{\max}$, the friction force increases strongly with increasing cutoff. The highest cutoff we consider is $k_{\max} = 70\ \text{nm}^{-1}$ which via the simple relation $k_{\max} = \pi/R$ corresponds to a radial cutoff of $R = 0.05$ nm; clearly, for higher wave vectors we expect the point-charge model employed in our classical MD simulations to become inaccurate. The friction force curves in Fig. 9(a) for the higher wave vector cutoffs exhibit a maximal value at a velocity around $v = 300$ m/s and slowly decay for larger velocities. This is reminiscent of the pronounced velocity dependencies encountered for the Stokes friction of a moving sphere in a viscous solvent when described by the linearized frequency-dependent Navier-Stokes equation.[43]

The concept of dielectric friction has a long history,[17,18] but note that previous simulation estimates for the friction of a moving charge in water used approximate theories and

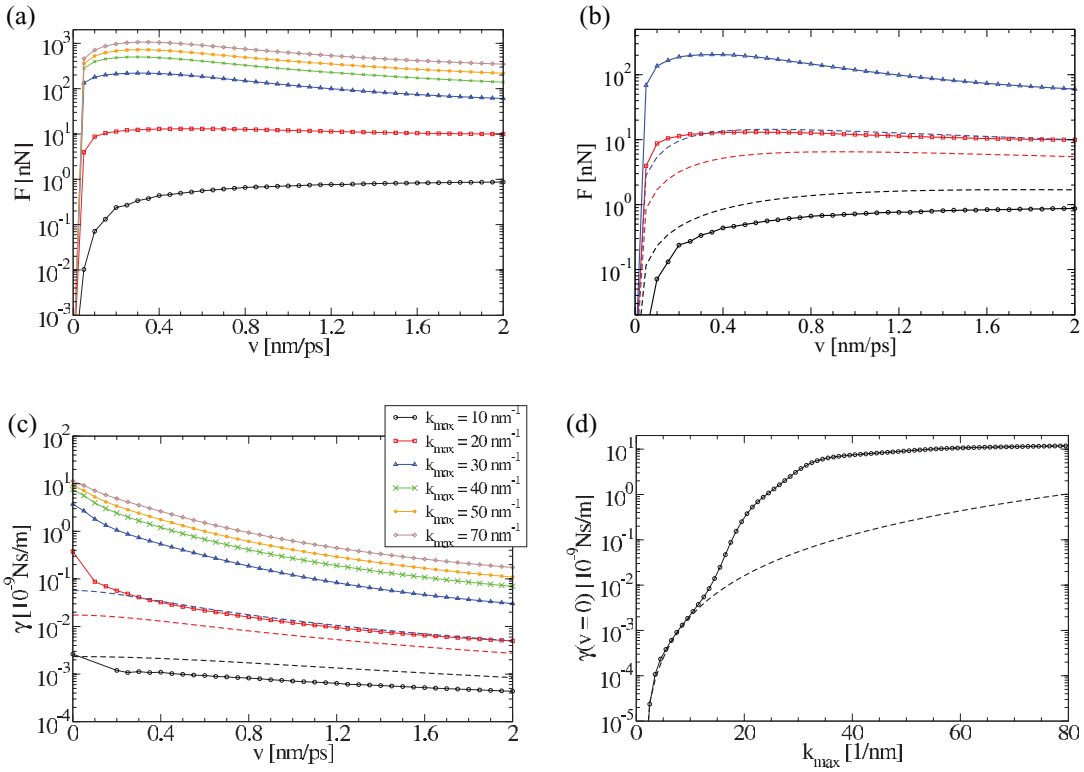

FIG. 9. (a) and (b) Drag force F and (c) friction coefficient $\gamma = F/v$ of a charged particle with charge $q_0 = e$ as a function of the particle velocity v as obtained by Eq. (28) (open symbols and solid lines). Different symbol shapes and line colors denote results for different values of the upper wave vector cutoff $k_{\max}$. In (b) and (c) in addition results obtained using the single Debye peak approximation, Eq. (33), with $\varepsilon(0) = 80$, $\varepsilon(\infty) = 1$, and $\tau = 10$ ps are shown (dashed lines). (d) Comparison of the friction coefficient in the limit $v \to 0$ as a function of the wave vector cutoff $k_{\max}$ in Eq. (29) using the full susceptibility from the MD simulations (open symbols and solid lines) with the single Debye peak approximation, Eq. (35) (dashed line). The dynamic charge-charge structure factor used in the calculation is taken from SPC/E water at $T = 300$ K and $p = 1$ bar.

therefore did not resolve the velocity dependence of the friction force in full detail.[44] Although it is clear that the dielectric and non-electrostatic friction contributions are for the case of ions moving through water intimately coupled and difficult to disentangle,[45] the decrease of friction with increasing velocity is certainly noteworthy and points to collective effects. In fact, for electrons in water, one would expect non-electrostatic friction effects to be rather small and therefore the results predicted in Fig. 9(a) to be more directly applicable. In Fig. 9(c) we plot the friction coefficient $\gamma = F/v$ as a function of the velocity for the same values of the upper wave vector cutoff $k_{\max}$ (solid lines) and observe a monotonic decay and again a strong dependence on the value of $k_{\max}$.

We note that in the limit of $v \to 0$ Eq. (28) simplifies and the friction coefficient is given by

$$\gamma(v=0) = -\frac{2}{3}\frac{q_0^2\rho}{4\pi\varepsilon_0^2 k_B T}\int_0^{k_{\max}} dk S_{qq}(k,0) \tag{29}$$

and takes on a finite value, as seen in Fig. 9(c).

C. Limitations of the single Debye-peak approximation and break-down of linear response theory

To understand the strong cutoff dependence of the calculated friction forces and friction coefficients in Figs. 9(a) and 9(c) it is useful to compare our results to the limiting case of a single Debye relaxation mode, in which limit the calculation can be done exactly.[17,18] First we note that the standard electrodynamic relations between the polarization density P, the displacement field D, and the electric field E, namely, $D = P + \varepsilon_0 E$ and $D = \varepsilon_0\varepsilon E$, yield in comparison with our definition for the susceptibility in Eq. (10) the relation

$$\chi(k,\omega) = 1 - \varepsilon^{-1}(k,\omega). \tag{30}$$

For the imaginary part of the susceptibility this leads to

$$\chi''(k,\omega) = \frac{\varepsilon''(k,\omega)}{|\varepsilon(k,\omega)|^2}. \tag{31}$$

The standard Debye model for the dielectric response of a solution neglects the wave-vector dependence and reads

$$\varepsilon(\omega) = \frac{\varepsilon(0)-\varepsilon(\infty)}{1-i\omega\tau} + \varepsilon(\infty). \tag{32}$$

It describes a single relaxation mode with relaxation time τ. We thus obtain

$$\chi''(\omega) = \frac{\omega\tau(\varepsilon(0)-\varepsilon(\infty))}{\varepsilon^2(0)+\varepsilon^2(\infty)(\omega\tau)^2}. \tag{33}$$

We note that while $\varepsilon''(\omega)$ has a maximum at $\omega = \tau^{-1}$, the maximum of $\chi''(\omega)$ is shifted to higher frequencies and occurs at $\omega = (\varepsilon(0)/\varepsilon(\infty))\tau^{-1}$. Inserting the single-Debye approximation Eq. (33) into the expression Eq. (27) we obtain an approximation for the friction force F. Choosing $\varepsilon(0) = 80$ as appropriate for the static dielectric constant of SPC/E water, choosing the dielectric constant in the optical to equal the vacuum value $\varepsilon(\infty) = 1$, which reflects the absence of high-frequency polarization effects in the MD simulations, and a relaxation time of $\tau = 10$ ps, which again is close to the actual relaxation time in SPC/E water, we obtain via numerical integration of Eq. (27) the broken lines in Fig. 9(b) which correspond to three different values of the upper momentum cutoff $k_{\max}$. It is seen that for the smallest value $k_{\max} = 10\ \mathrm{nm}^{-1}$ denoted by a black broken line, the deviation from the result using the full susceptibility from the MD simulations (black circles and black solid line) is quite modest, but grows significantly for $k_{\max} = 20\ \mathrm{nm}^{-1}$ (red broken line and red data points) and for $k_{\max} = 30\ \mathrm{nm}^{-1}$ (blue broken line and blue data points). In Fig. 9(c) we show the single-Debye peak approximation for the friction coefficient $\gamma = F/v$ as a function of the velocity for the three smallest values of the upper wave vector cutoff $k_{\max}$ (broken lines). We again observe that for the smallest value $k_{\max} = 10\ \mathrm{nm}^{-1}$ (black broken line), the agreement with the result using the full susceptibility from the MD simulations (black circles and black solid line) is quite good, but significant deviations are seen for $k_{\max} = 20\ \mathrm{nm}^{-1}$ (red broken line and red data points) and for $k_{\max} = 30\ \mathrm{nm}^{-1}$ (blue broken line and blue data points).

In the limit of vanishing velocity of the point charge, $v \to 0$, the expression for the friction coefficient using the single-Debye peak approximation can be calculated in closed form and reads

$$\gamma(v=0) = -\frac{1}{18\pi^2}\frac{q_0^2(\varepsilon(0)-\varepsilon(\infty))\tau k_{\max}^3}{\varepsilon_0\varepsilon^2(0)}. \tag{34}$$

Approximating $\varepsilon(0) - \varepsilon(\infty) \approx \varepsilon(0)$, defining the Bjerrum length as $\ell_B = q_0^2/(4\pi\varepsilon_0\varepsilon(0)k_B T)$ which for a unit charge $q_0 = e$ has a value of roughly $\ell_B \approx 1$ nm, and relating the upper cutoff to an effective radius R as $k_{\max} = \pi/R$, we obtain the simple expression

$$\gamma(v=0) = -\frac{2}{9\pi}\ell_B k_B T \tau k_{\max}^3 = -\frac{2\pi^2}{9}\frac{\ell_B k_B T \tau}{R^3}, \tag{35}$$

which has the same scaling and a very similar numerical prefactor as previously derived expressions.[17,18] The cubic dependence of the friction coefficient on the upper wave vector cutoff $k_{\max}$ explains why the data in Fig. 9 depend so sensitively on $k_{\max}$. Putting in numbers which presumably are appropriate for electrons in water, i.e., $\ell_B = 1$ nm, $\tau = 10$ ps, $k_B T = 4 \times 10^{-21}$ J, $k_{\max} = \pi/R = 10^{10}\ \mathrm{m}^{-1}$, we obtain the value $\gamma(v=0) \approx 2 \times 10^{-12}$ N s/m. Through Einstein's relation $D = k_B T/\gamma$ we obtain a diffusion constant of $D \approx 2 \times 10^{-9}\ \mathrm{m}^2/\mathrm{s} = 2 \times 10^{-5}\ \mathrm{cm}^2/\mathrm{s}$, which agrees well with experimental results for the electron diffusivity[46] and previous theoretical estimates.[17,18] Incidentally, an estimate of the hydrodynamic friction for a particle with a radius $R = 0.1$ nm gives, using Stokes' law with a water viscosity of $\eta = 10^{-3}$ kg/(m s), a friction coefficient of $\gamma_{\mathrm{hyd}} = 6\pi\eta R = 2 \times 10^{-12}$ N s/m which is identical to the dielectric friction estimate. This reflects that dielectric and hydrodynamic friction effects have very similar magnitudes for liquid water if the characteristic radii are chosen similarly and of the order of $R = 0.1$ nm. The static friction coefficient $\gamma(v=0)$ according to Eq. (35) is shown in Fig. 9(d) as a function of $k_{\max}$ by a broken line and compared to the result using the full susceptibility in Eq. (29) (solid line and symbols). It is seen that for $k_{\max} < 10\ \mathrm{nm}^{-1}$ the two calculations agree while for larger values of $k_{\max}$ the single Debye peak approximation

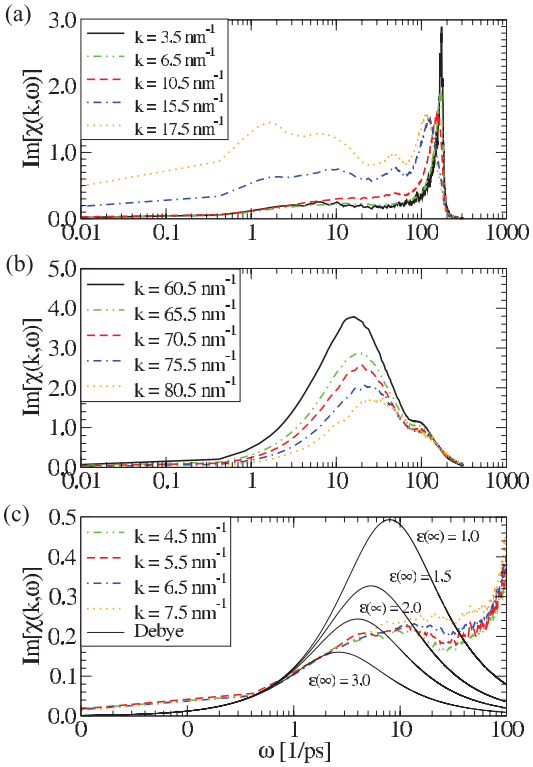

FIG. 10. Imaginary part of the longitudinal response function $\mathrm{Im}[X_{||}(k, \omega)]$ calculated from the dynamic charge-charge structure factor by Eq. (15) for (a) small and (b) large wave vectors k. In (c) a comparison with the Debye form, Eq. (33), for small wave vectors k and small frequencies ω is shown. Note that while the dielectric function has a maximum at $\omega = \tau^{-1}$, the maximum of $\chi''(\omega)$ is shifted to higher frequencies and occurs at $\omega = (\varepsilon(0)/\varepsilon(\infty))\tau^{-1}$. The dynamic charge-charge structure factor used in the calculation is taken from SPC/E water at $T = 300$ K and $p = 1$ bar.

underestimates $\gamma(v = 0)$ by roughly an order of magnitude. To understand the cause of this deviation in more detail, we show in Figs. 10(a) and 10(b) the susceptibility $\chi''_{||}(k, \omega)$ for different fixed values of k as a function of ω. It is seen that for small values of k at $\omega \approx 175$ ps^{-1} a sharp peak is present, which by comparison with the results for S_{qq} in Fig. 2 is traced back to the fast librational motion of the hydrogen atoms. Figure 10(c) compares $\chi''_{||}(k, \omega)$ in the small ω-region with the Debye form, Eq. (33), for a few different values of $\varepsilon(\infty)$. The overall agreement is not impressive, but the comparison shows that the small hump in $\chi''_{||}(k, \omega)$ around $\omega \approx 10$ ps^{-1} is related to the dielectric Debye relaxation which only becomes accurate in the limit $k \to 0$. We conclude that the strong deviations in $\chi''_{||}(k, \omega)$ at finite values of k from the simple Debye form lead to the pronounced deviations between the results based on the numerical integration over the full $\chi''_{||}(k, \omega)$ and the single-Debye peak approximation in Fig. 9.

We finally want to explain how the upper wave vector cutoff $k_{\max}$ can be derived for a toy model of a charge distribution with a finite radius R. Considering a moving external charge that is distributed over a spherical shell with a radius R,

$$q_{\mathrm{ext}}(\vec{r}, t) = \frac{q_0}{4\pi R^2}\delta(|\vec{r} - \vec{v}t| - R), \tag{36}$$

the analogous calculation leading to the friction force, Eq. (28), gives for the present case of a charged spherical shell the friction force

$$F = -\frac{q_0^2 \rho v}{4\pi \varepsilon_0^2 k_{\mathrm{B}} T}\int_{-1}^{1} ds \int_0^{\infty} dk s^2 S_{qq}(k, kvs) J_0^2(kR), \tag{37}$$

where $J_0(x) = \sin x/x$ is the first spherical Bessel function. For vanishing sphere radius $R \to 0$ we recover the previous result from Eq. (28), but for finite R the squared Bessel function in the integral leads to fast convergence of the momentum integration, so that the upper integration boundary can be set to infinity. In an approximate way, the Bessel function can be thought of as imposing a smooth upper momentum cutoff at a value of roughly $k_{\max} \approx \pi/R$, so that the two expressions, Eqs. (28) and (37), are in fact equivalent.

It remains to be discussed why we need to impose a rather small upper cutoff $k_{\max} = \pi/R = 10^{10}$ m^{-1} in order to obtain a value for the friction coefficient that roughly matches the experimental one for an electron. In fact, the need to impose a cutoff $k_{\max}$ comes mainly from a breakdown of the assumption of linear response theory (in addition, the susceptibility obtained with the point charge SPC/E water model is also inaccurate at high momentum, but this effect is of secondary importance). As is easy to see, the electric charge of an electron is too large for linear response to hold and as a result of the strong polarization of the hydration water, a dielectrically saturated shell forms around the point charge with a radius of a few water molecules. Outside this radius linear response theory applies. A simple approximate remedy to this issue is to use a heuristic cutoff, leading to Eq. (28), or to consider the friction force on a charged shell with a radius R corresponding roughly to the dielectrically saturated region, leading to Eq. (37).

V. ELECTRO-ACOUSTIC COUPLING

As demonstrated by the structure factors shown in Figs. 3 and 8, there is a finite coupling between the particle and the charge density, which means that electro-acoustic coupling is present in pure water: An alternating electric field thus produces a pressure wave and vice versa. This coupling can be quantified by the response function $\Phi_{\mathrm{UVP}}(k, t)$, which relates the ultrasonic vibration potential $\phi(k, t)$ to the longitudinal component of the mass current density, $j_{m,||}(k, t) = (k_v/k) j_v(k, t)$, induced by an applied sound wave, where $\vec{j}(k, t) = \sum_{i,\alpha} m_\alpha \vec{v}_i^{\alpha} e^{-i\vec{k}\vec{r}_i^{\alpha}}$ and m_α is the mass of the atomic site $\alpha = \mathrm{O}, \mathrm{H}$,

$$\phi(k, t) = \int_{-\infty}^{t} dt' \Phi_{\mathrm{UVP}}(k, t - t') \frac{1}{\rho_m V} j_{m,||}(k, t'). \tag{38}$$

The Fourier transform of the UVP response function is defined as

$$\Phi_{\mathrm{UVP}}(k, \omega) = \int_0^{\infty} dt \Phi_{\mathrm{UVP}}(k, t) e^{i\omega t}. \tag{39}$$

Using linear response theory, Yamaguchi *et al.*[47] derived the following expression for $\Phi_{\mathrm{UVP}}(k, \omega)$, which depends on a combination of atomic site-site correlation functions and

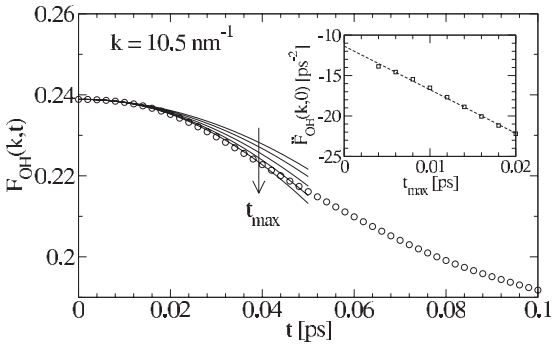

FIG. 11. Illustration of the fitting method used to obtain $\ddot{F}_{\alpha\beta}(k, 0)$ from $F_{\alpha\beta}(k, t)$ for the example of $F_{\mathrm{OH}}(k, t)$. Circles show $F_{\mathrm{OH}}(k, t)$ for $k = 10.5$ nm^{-1}; solid lines are quadratic fits to $F_{\mathrm{OH}}(k, t)$ for $t < t_{\max}$ and $t_{\max} = 0.004$, 0.008, 0.012, 0.016, and 0.02 ps. In the inset the curvature $\ddot{F}_{\alpha\beta}(k, 0)$ of the quadratic fits is plotted as a function of $t_{\max}$ (squares) including a linear extrapolation (dashed line).

structure factors,

$$\Phi_{\mathrm{UVP}}(k, \omega) = \frac{\rho_m e \sum_{\alpha,\beta} m_\alpha z_\beta H_{\alpha\beta}(k, \omega)}{\epsilon_0 \omega k \sum_{\alpha,\beta} m_\alpha m_\beta H_{\alpha\beta}(k, \omega)}, \tag{40}$$

where

$$H_{\alpha\beta}(k, \omega) = -\ddot{F}_{\alpha\beta}(k, 0) + \omega^2 S_{\alpha\beta}(k) + i\pi\omega^3 S_{\alpha\beta}(k, \omega). \tag{41}$$

We determine the second time derivative $\ddot{F}_{\alpha\beta}(k, 0)$ by fitting $F_{\alpha\beta}(k, t)$ with a quadratic function on the interval $[0, t_{\max}]$ for several values of $t_{\max} < 0.02$ ps. The curvature at $t = 0$ is then obtained by extrapolating the resulting curvatures linearly to $t_{\max} \to 0$, as illustrated in Fig. 11. Figure 12 shows the absolute value of the UVP response function $\Phi_{\mathrm{UVP}}(k, \omega)$ in the (k, ω)-plane. The plot in Figure 12(b) for low ω values demonstrates that the coupling is most pronounced at frequencies below the dispersion relation for propagating normal sound waves. In most practical applications, though, this effect will be probed by ordinary sound waves. In Fig. 13 we therefore plot the absolute value and the argument of $\Phi_{\mathrm{UVP}}(k, \omega)$ along the dispersion relation $\omega(k) = c_s k$ using the hydrodynamic (adiabatic) sound velocity $c_s = 1510$ m/s. The maximum value of $|\Phi_{\mathrm{UVP}}(k, \omega)|$ is of the order of 1 mV/(m s) at the smallest wave vectors considered by us and decays strongly for increasing wave vectors. The relationship

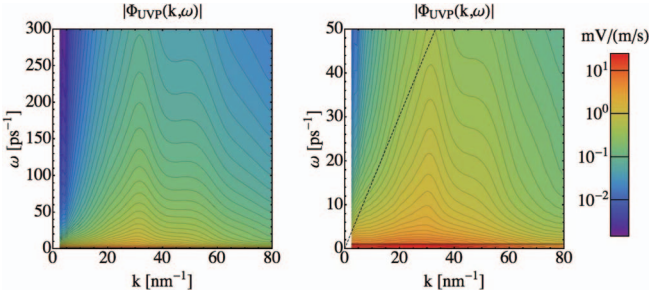

FIG. 12. *Left panel:* Semilogarithmic plot of the absolute value of the UVP response function $\Phi_{\mathrm{UVP}}(k, \omega)$ of SPC/E water at $T = 300$ K and $p = 1$ bar. *Right panel:* Close-up view of the low ω region. The dashed dotted line marks the dispersion relation $\omega(k) = c_s k$, with the adiabatic sound velocity $c_s = 1510$ m/s of SPC/E water.

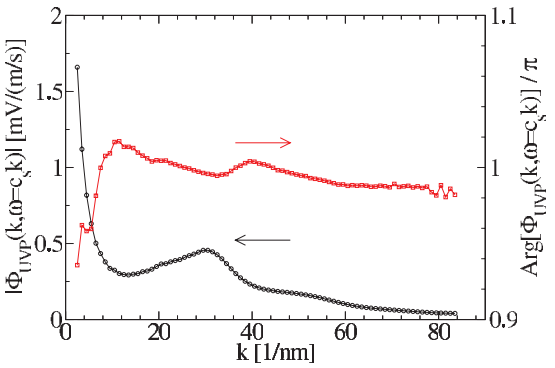

FIG. 13. Absolute value (black circles, left scale) and argument (red squares, right scale) of the UVP response function $\Phi_{\mathrm{UVP}}(k, \omega)$ of SPC/E water at $T = 300$ K and $p = 1$ bar along the dispersion relation $\omega(k) = c_s k$, with the adiabatic sound velocity $c_s = 1510$ m/s.

between the velocity amplitude u and the pressure amplitude p in a sound wave is given by the acoustic impedance $Z = \rho_{\mathrm{m}} c_s$ via[48]

$$p = Zu. \tag{42}$$

For SPC/E water with $c_s = 1510$ m/s and $\rho_{\mathrm{m}} = 1000$ kg/m^3 we have $Z = 1.5$ MPa s/m. To reach a velocity amplitude of 1 cm/s we accordingly need a pressure amplitude of ≈1500 Pa which corresponds to ≈160 dB, which is a large but experimentally reachable value.[11] Approximating the parameter combination $j_{m,||}/\rho_m V$ in Eq. (38) by the velocity of 1 cm/s, and using as an estimate for the UVP coupling term $|\Phi_{\mathrm{UVP}}(k, \omega)| = 1$ mV/(ms), we arrive at an induced potential of the order of ≈10 μV, which is non-negligible. As a word of caution we note that the range of wave vectors and frequencies accessible to MD simulations is far beyond the regime of ordinary sound waves. The value for the induced potential obtained by us is thus merely a lower bound, since the UVP coupling coefficient $|\Phi_{\mathrm{UVP}}(k, \omega)|$ increases strongly for smaller wave vectors, as can be seen in Fig. 13.

VI. CONCLUSIONS

Using classical MD simulations of the SPC/E water model at ambient pressure and room temperature, we determine the auto- and cross-correlation functions and associated dynamic structure factors of the oxygen and hydrogen sites in liquid water over a wide range of wave vectors and frequencies. Based on the diagonal and off-diagonal structure factors involving mass and charge densities we consider dielectric friction and electro-acoustic coupling effects in liquid water.

On the linear-response level, the friction force on a moving point charge is maximal at a velocity around $v = 300$ m/s and decays for larger velocities. This quasi-resonant friction feature is reminiscent of frequency-dependent Stokes' friction, which also shows deviations from a linear velocity dependence. Although our calculation is strictly valid only on the linear-response level and thus neglects the nonlinear effects the presence of a point charge has on the water surrounding, this finding is interesting and points to complex dynamic phenomena for moving charges in liquid water. This

might be even biologically relevant for electron and proton charge-transfer processes in proteins. In situations where the dielectric adsorption spectrum has features at lower frequencies than in bulk water, such as in water-filled protein cavities or close to membrane-water interfaces, we expect the velocity of maximal friction to be shifted to lower values. The friction forces we calculate are for elevated momentum cutoff values considerably larger than predicted by the single Debye relaxation mode approximation, which is due to non-Debye-like resonances related to librations at high frequencies in the simulated water susceptibility. For an electron a sufficiently low momentum cutoff basically eliminates the high-frequency domain, which can be thought of as to account for dielectric saturation effects in a heuristic manner. However, non-Debye effects can be relevant for the kinetics and motion of partial molecular charges which do not lead to dielectric saturation at small length scales (i.e., high momenta). We note that in the high-wave vector/high frequency regime classical MD simulations become unreliable as polarization and quantum effects start to be important, therefore in this regime our results should be merely viewed as indicative.

The coupling between electrostatic and acoustic phenomena leads to two well-known effects: an ultrasonic wave induces an alternating electrostatic potential, the so-called ultrasonic vibration potential ϕ_{UVP} and conversely an acoustic wave is produced by the application of a time-varying electric field, quantified by the electrokinetic sonic amplitude. The question whether pure water generates a finite UVP was unsettled. Using the charge-mass dynamic structure factor we derive an explicit value for the UVP and thus for the electro-acoustic conversion coefficient in liquid water. For SPC/E water we estimate that for a velocity amplitude of 1 cm/s, which corresponds to a pressure amplitude of $\approx$1500 Pa or 160 dB, the induced electrostatic potential is of the order of $\approx 10\ \mu$V at a wave vector of about $k = 1\ \mathrm{nm}^{-1}$. This value is expected to increase strongly for smaller wave vectors, and should therefore be understood as a lower bound or proof of concept. In the future, it will be interesting to perform similar studies at aqueous interfaces, where electro-acoustic conversion effects could be enhanced by interfacial water ordering and confinement effects.

ACKNOWLEDGMENTS

The authors acknowledge financial support from the DFG within SFB 1078.

[1]J. M. Sorenson, G. Hura, R. M. Glaeser, and T. Head-Gordon, J. Chem. Phys. **113**, 9149 (2000).
[2]T. Head-Gordon and G. Hura, Chem. Rev. **102**, 2651 (2002).
[3]J. Wang, A. N. Tripathi, and V. H. Smith, J. Chem. Phys. **101**, 4842 (1994).
[4]R. Coridan, N. Schmidt, G. Lai, R. Godawat, M. Krisch, S. Garde, P. Abbamonte, and G. Wong, Phys. Rev. Lett. **103**, 237402 (2009).
[5]R. H. Coridan, N. W. Schmidt, G. H. Lai, P. Abbamonte, and G. C. L. Wong, Phys. Rev. E **85**, 031501 (2012).
[6]J. P. Hansen and I. R. McDonald, *Theory of Simple Liquids*, 3rd ed. (Academic Press, Amsterdam, 2006).
[7]R. Kubo, J. Phys. Soc. Jpn. **12**, 570 (1957).
[8]H. A. Bethe, Ann. Phys. **397**, 325 (1930).
[9]P. Debye, J. Chem. Phys. **1**, 13 (1933).
[10]E. Yeager, J. Bugosh, F. Hovorka, and J. McCarthy, J. Chem. Phys. **17**, 411 (1949).
[11]R. Zana and E. Yeager, J. Phys. Chem. **71**, 521 (1967).
[12]A. Hunter and T. Jones, Proc. Phys. Soc., London **80**, 795 (1962).
[13]A. Hunter, Proc. Phys. Soc., London **71**, 847 (1958).
[14]A. Weinman, Proc. Phys. Soc., London **73**, 345 (1959).
[15]A. Weinman, Proc. Phys. Soc., London **75**, 102 (1960).
[16]T. Oja, G. Pedersen, and D. Cannon, U.S. Patent 4,497,208 (February 5, 1985).
[17]R. Zwanzig, J. Chem. Phys. **52**, 3625 (1970).
[18]J. Hubbard, J. Chem. Phys. **68**, 1649 (1978).
[19]B. Hess, C. Kutzner, D. van der Spoel, and E. Lindahl, J. Chem. Theory Comput. **4**, 435 (2008).
[20]D. van der Spoel, E. Lindahl, B. Hess, G. Groenhof, A. E. Mark, and H. J. C. Berendsen, J. Comput. Chem. **26**, 1701 (2005).
[21]H. J. C. Berendsen, J. R. Grigera, and T. P. Straatsma, J. Phys. Chem. **91**, 6269 (1987).
[22]H. J. C. Berendsen, J. Postma, W. F. van Gunsteren, A. Dinola, and J. Haak, J. Chem. Phys. **81**, 3684 (1984).
[23]U. Essmann, L. Perera, M. L. Berkowitz, T. Darden, H. Lee, and L. Pedersen, J. Chem. Phys. **103**, 8577 (1995).
[24]T. Darden, D. York, and L. Pedersen, J. Chem. Phys. **98**, 10089 (1993).
[25]M. P. Allen and D. J. Tildesley, *Computer Simulation of Liquids*, 1st ed. (Oxford University Press, Oxford, 1987).
[26]S. Miyamoto and P. A. Kollmann, J. Comput. Chem. **13**, 952 (1992).
[27]B. Ladanyi and B. Perng, AIP Conf. Proc. **492**, 250 (1999).
[28]I. P. Omelyan, Mol. Phys. **93**, 123 (1998).
[29]P. Bopp, A. Kornyshev, and G. Sutmann, J. Chem. Phys. **109**, 1939 (1998).
[30]I. M. Svishchev and P. G. Kusalik, J. Chem. Soc. Faraday Trans. **90**, 1405 (1994).
[31]G. Ruocco and F. Sette, Condens. Matter Phys. **11**, 29 (2008).
[32]F. Sedlmeier, D. Horinek, and R. R. Netz, J. Am. Chem. Soc. **133**, 1391 (2011).
[33]F. H. Stillinger and A. Rahman, J. Chem. Phys. **60**, 1545 (1974).
[34]A. Rahman and F. H. Stillinger, Phys. Rev. A **10**, 368 (1974).
[35]J. Teixeira, M. Bellissent-Funel, S. Chen, and B. Dorner, Phys. Rev. Lett. **54**, 2681 (1985).
[36]F. Sette, G. Ruocco, M. Krisch, U. Bergmann, C. Masciovecchio, V. Mazzacurati, G. Signorelli, and R. Verbeni, Phys. Rev. Lett. **75**, 850 (1995).
[37]F. Sette, G. Ruocco, M. Krisch, C. Masciovecchio, R. Verbeni, and U. Bergmann, Phys. Rev. Lett. **77**, 83 (1996).
[38]G. Ruocco, F. Sette, U. Bergmann, M. Krisch, C. Masciovecchlo, V. Mazzacurati, G. Signorelli, and R. Verbeni, Nature **379**, 521 (1996).
[39]U. Balucani, G. Ruocco, A. Torcini, and R. Vallauri, Phys. Rev. E **47**, 1677 (1993).
[40]F. Sciortino and S. Sastry, J. Chem. Phys. **100**, 3881 (1994).
[41]T. Komatsu, N. Yoshii, S. Miura, and S. Okazaki, Fluid Phase Equilib. **226**, 345 (2004).
[42]L. D. Landau and E. M. Lifshitz, *Electrodynamics of Continuous Media*, 2nd ed. (Pergamon Press, Oxford, 1984)
[43]A. Erbas, R. Podgornik, and R. R. Netz, Eur. Phys. J. E **32**, 147 (2010).
[44]M. Bruehl and J. T. Hynes, J. Phys. Chem. **96**, 4068 (1992).
[45]P. Kumar and M. Maroncelli, J. Chem. Phys. **112**, 5370 (2000).
[46]J. Schnitker and P. J. Rossky, J. Phys. Chem. **93**, 6965 (1989).
[47]T. Yamaguchi, T. Matsuoka, and S. Koda, J. Chem. Phys. **119**, 4437 (2003).
[48]R. H. Randall, *An Introduction to Acoustics*, 1st ed. (Addison Wesley, Cambridge, 1951).